

Observation of wind-waves from a moored buoy in the Southern Ocean

Henrique Rapizo¹ · Alexander V. Babanin¹ · Eric Schulz² · Mark A. Hemer³ · Tom H. Durrant⁴

Received: 3 July 2015 / Accepted: 26 August 2015 / Published online: 11 September 2015
© Springer-Verlag Berlin Heidelberg 2015

Abstract The Southern Ocean is an important component in the global wave climate. However, owing to a lack of observations, our understanding of waves is poor compared to other regions. The Southern Ocean Flux Station (SOFS) has been deployed to fill this gap and represents the first successful moored air-sea flux station at these southern hemisphere latitudes. In this paper, we present for the first time the results from the analysis of the wave measurements, focused on statistics and extremes of the main wave parameters. Furthermore, a spectral characterization is performed regarding the number of wave systems and predominance of swell/wind-sea. Our results indicate a high consistency in terms of wave parameters for all deployments. The maximum significant wave height obtained in the 705 days of observation was 13.41 m. The main spectra found represent unimodal swell dominated cases; however, the dimensionless energy plotted against dimensionless peak frequency for these spectra follows a well-known relation for wind-sea conditions. In addition, the Centre for Australian Weather

and Climate Research wave hindcast is validated with the SOFS data.

Keywords Wind-generated waves · Wave parameters · Wave spectrum · Spectral partitioning · Wave hindcast

1 Introduction

The Southern Ocean (SO) is the southern-most part of the global ocean and represents around 22 % of the sea surface area. This region is known to play an important role in the climate system, cycling heat, carbon, and nutrients (e.g., Orsi et al. 1999). Waves modulate the air-sea fluxes (Badulin et al. 2007) and exchanged properties are redistributed primarily via the Antarctic Circumpolar Current (Rintoul and Sokolov 2001). Additionally, the high latitude and absence of land barriers allow strong winds to blow over practically unlimited fetches, creating ideal conditions for severe wave generation. The waves generated in this region have far reaching effects, contributing significantly to the wave climate in all the major ocean basins (Alves 2006).

Our interest in the Southern Ocean is from an air-sea interaction perspective, recognizing that wave development under strong wind forcing is likely to be different from moderate conditions (Powell et al. 2003; Donelan et al. 2006). The effects of waves on the lower atmosphere and momentum exchange in the air-sea boundary layer are modulated by the surface wave characteristics (e.g., Badulin et al. 2007); however, this complex coupled system is still poorly understood and highly parameterized. The long fetches and the relative constant high wind speed make the SO an interesting area to study wave evolution under extreme weather.

Responsible Editor: Bruno Castelle

✉ Henrique Rapizo
hrapizo@swin.edu.au

¹ Centre for Ocean Engineering, Science and Technology, Swinburne University of Technology, PO Box 218, Melbourne, Victoria 3122, Australia

² Australian Bureau of Meteorology, Melbourne, Victoria, Australia

³ CSIRO Oceans and Atmosphere Flagship, Hobart, Tasmania, Australia

⁴ MetOcean Solutions, Raglan, New Zealand

Due to the harsh ocean environment and remote location, there is a lack of air-sea fluxes and direct wave measurements in the SO. It is amongst the poorest sampled of all oceans, and this leads to large uncertainties in the global air-sea flux and wave climatology. Little is known about the wave characteristics in the SO other than by mean monthly satellite climatologies (e.g., Mognard et al. 1983; Young 1994; Hemer et al. 2009; Hemer 2010), which are limited to significant wave heights, or wave model data. Wave hindcasts provide a tool to map wave parameters globally; however, the results are unvalidated. Deep ocean moored wave buoys are the most reliable source of wave measurement to validate satellite altimeter and wave model data, and the analysis methods have been well established for decades.

The Southern Ocean Flux Station (SOFS) was established as part of the Southern Ocean Time Series (SOTS) project (Trull et al. 2010) under the Australian Integrated Marine Observing System (IMOS) (Meyers 2008) with the aim of proving better understanding of the SO through a variety of meteo-oceanographic observations. Five deployments have been performed since March 2010. The third deployment at the beginning of 2013 was short-lived due to technical issues and is excluded from this study. Excluding the current (SOFS-5) deployment also, the three remaining deployments provide measurements spanning a period over 705 days. The approximate coordinates of the mooring location was 47° S and 142° E (Fig. 1). Table 1 contains details of each deployment.

The target deployment period is 12 months. Due to the harsh and remote SO location, the SOFS design faces significant technical challenges. Wind, waves, and currents create high physical stress on the mooring structure. Schulz et al. (2011) describe the dynamic fatigue analysis for the SOFS design that uses wave information. More detailed

Table 1 Details of the SOFS deployments

Deployment	Location	Period	Wave sensors
SOFS-1	46.723 S 141.870 E	Mar 2010 to Jan 2011	MRU
SOFS-2	46.772 S 141.980 E	Nov 2011 to Jul 2012	MRU and TriAxys
SOFS-4	46.777 S 141.993 E	Apr 2013 to Oct 2013	MRU and TriAxys

SOFS-3 was excluded from the analysis due to technical issues

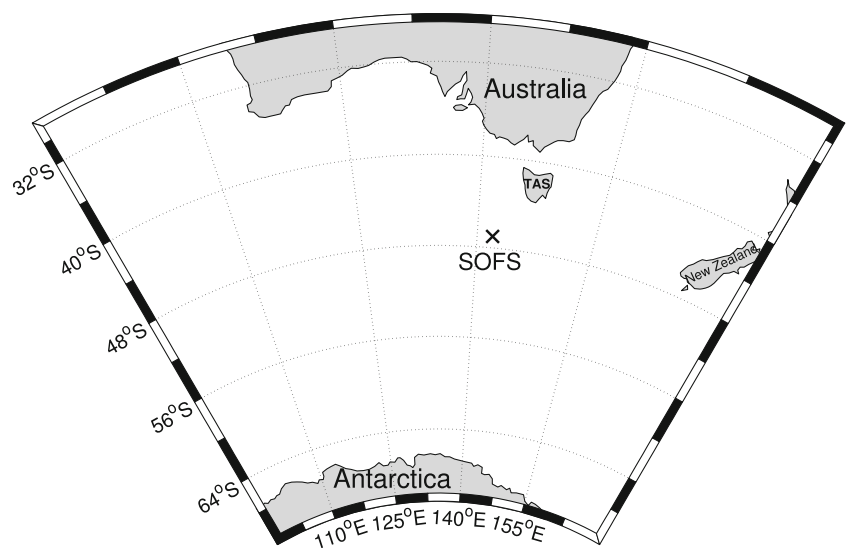
information about the mooring as well as a description of the overall sensors installed can be found in Schulz et al. (2012). Figure 2 illustrates the slack-mooring system and location of instruments. This study presents for the first time the results of the wave data analysis for the three successful deployments. Statistics and distribution of the wave parameters are shown and discussed (Section 3.1). The wave spectra are characterized by number of wave systems and predominance of swell or wind-sea (Section 3.2). We also present a validation of the Centre for Australian Weather and Climate Research (CAWCR) wave hindcast: A partnership between the Bureau of Meteorology and CSIRO (Durrant et al. 2013) against the observations (Section 3.3).

2 Methods

2.1 Data analysis and wave parameters

Wave parameters were obtained from two different sensors: a system based on a in-house motion reference unit (MRU) developed at the CSIRO, using the Microstrain 3DM-GX1

Fig. 1 Location of the Southern Ocean Flux Station (SOFS)



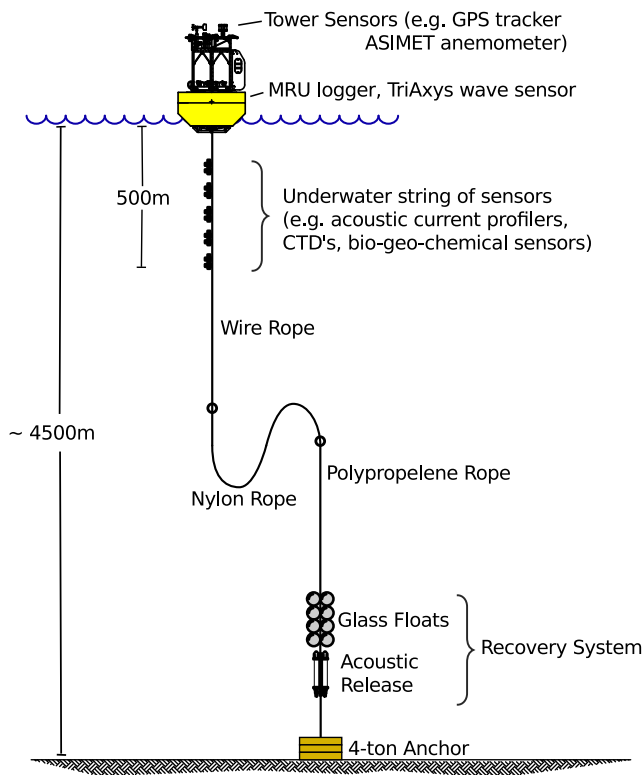


Fig. 2 Schematic of the slack-mooring system and location of instruments of the SOFS. Adapted from the CSIRO Fourth Deployment scope

sensor and configured to sample for the first 10 min of every hour at a 5 Hz sampling frequency, and the commercial TriAxys 3D accelerometer, configured to sample at 1.28 Hz over the first 20 min of every 2 h and provides the directional wave spectra. For both sensors, the wave spectrum is obtained from vertical acceleration in earth-coordinate system with 512 (MRU) and 128 (TriAxys)-point fast Fourier transforms (FFT) using the Welch method (Welch 1967). We have performed the spectral analysis for the MRU raw data only since the TriAxys sensor computes this internally and provides the frequency-directional spectra. The segment length applied in the spectral analysis of the MRU was chosen in order to obtain the same frequency resolution of 0.01 Hz provided by the TriAxys.

The vertical acceleration spectrum is converted to variance density spectrum of the surface elevation by:

$$S_D(f) = \frac{S_{AC}(f)}{\omega^4} \tag{1}$$

where $S_D(f)$ is the spectrum of the surface elevation, $S_{AC}(f)$ the spectrum of the surface vertical acceleration and ω the angular frequency. The large energy produced in low frequencies was removed by applying a filter based on a factor that represents the root-mean-square (RMS) accelerometer noise level.

A comparison between the spectra obtained from the MRU raw data and the TriAxys internal processing is shown in Fig. 3. Both directional spectra were calculated using the Maximum Entropy Method (Lygre and Krogstad 1986) for directional distribution. The agreement is good despite some differences in directional spreading. The double-peaked spectrum is well represented by both sensors as well as the integrated energy.

By calculating the wave spectrum, the main wave parameters commonly used to describe wave height and period can be obtained through the spectral moments:

$$H_{m0} = 4\sqrt{m_0} \approx H_s,$$

$$T_p = \frac{1}{f_p} = \frac{1}{f(S_{MAX})} \text{ and}$$

$$T_{m01} = \frac{m_0}{m_1}, \tag{2}$$

namely the zero-moment wave height, which approximates the average third most energetic waves of the record (H_s), the peak (T_p), and the mean period (T_{m01}). The spectral moments are defined:

$$m_n = \int_0^\infty f^n S(f) df \tag{3}$$

The mean wave direction is obtained from the first two Fourier coefficients:

$$\theta_0(f) = \arctan \left[\frac{b_1(f)}{a_1(f)} \right] \tag{4}$$

where a_1 and b_1 are obtained from the co- (C_{ij}) and quadrature (Q_{ij}) spectra (e.g., Benoit et al. 1997),

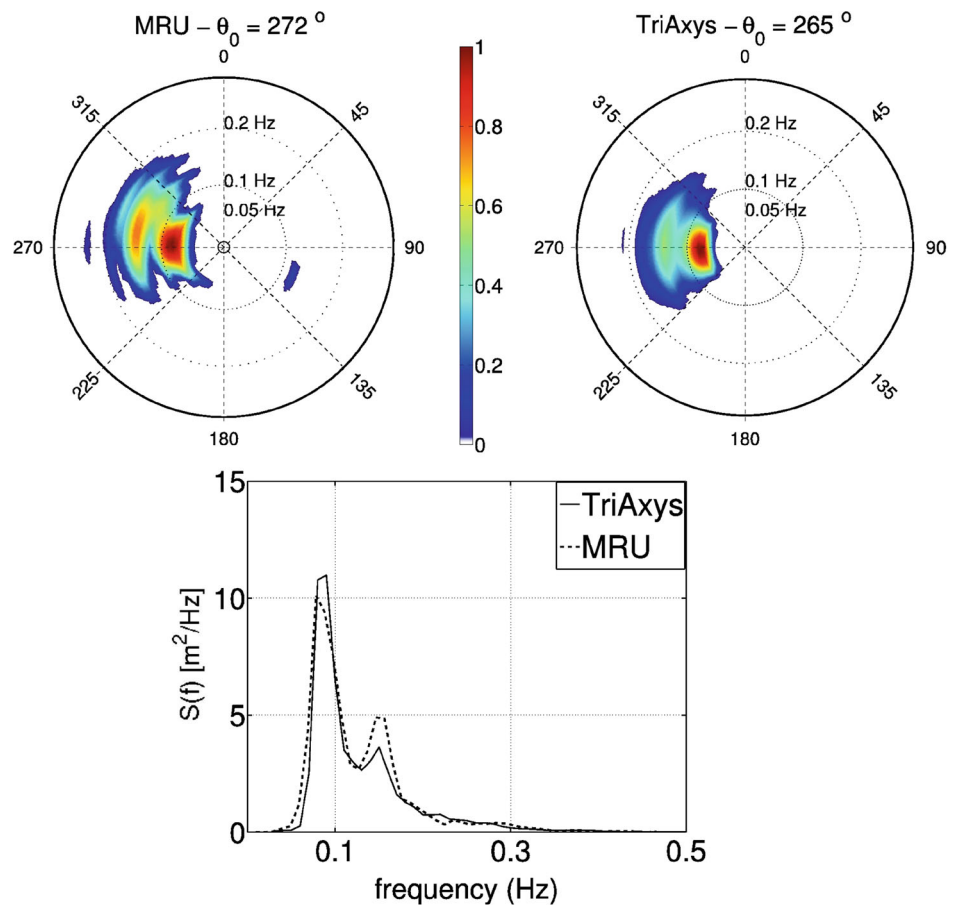
$$a_1(f) = \frac{Q_{12}}{kC_{11}} = \frac{1}{S(f)} \int_0^{2\pi} S(f, \theta) \cos \theta d\theta$$

$$b_1(f) = \frac{Q_{13}}{kC_{11}} = \frac{1}{S(f)} \int_0^{2\pi} S(f, \theta) \sin \theta d\theta \tag{5}$$

where k is wavenumber and the indices 1, 2, and 3 represent heave, east-west, and north-south slopes, respectively. The main directional parameter shown in this paper is the mean direction θ_0 corresponding to the peak period, hereinafter denoted as θ_p .

The MRU was the only wave sensor installed during the first deployment (SOFS-1). Schulz et al. (2011) tested the MRU sensor used against a Waverider buoy in a laboratory prior to this deployment, with very good agreement. For SOFS-2 and 4, we performed a comparison between the MRU and TriAxys, for H_{m0} and T_p , also with good agreement (Fig. 4). The obtained T_p had a lower correlation (0.92) than H_{m0} (0.98). The bias was very small for both parameters. For the deployments with both sensors installed, the TriAxys output is used instead of the MRU in this analysis because of the longer sampling time, which allows a better spectral estimation with higher confidence levels.

Fig. 3 Comparison of directional (*top*) and nondirectional (*bottom*) spectra between MRU and TriAxys for 16 February 2012. Directional spectrum is normalized by the maximum energy



2.2 Spectral partitioning

The wave parameters H_{m0} , T_p , and θ_p are commonly used to characterize the sea state. However, they are limited and

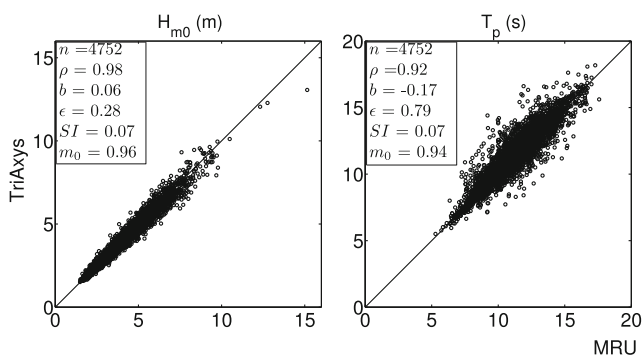


Fig. 4 Scatter plots of zero-moment wave height (H_{m0}) and peak period (T_p) for the MRU and TriAxys sensors. Displayed scatter statistics are n = number of samples, ρ = Pearson's correlation coefficient (Pearson 1896), b = bias in the TriAxys–MRU direction, ϵ = root mean square error, SI = scatter index, and m_0 = slope of least-square regression

do not describe all important wave properties. H_{m0} , for example, is obtained by integrating the spectrum over all frequencies and does not provide any information regarding the presence of different wave systems. To provide a better description of the waves in the SO, the wave spectra are analyzed individually and characterized by their number of wave systems, i.e., number of consistent partitions, and by the dominance of swell or wind-sea.

A number of different methodologies for spectral partitioning are available (e.g., Violante-Carvalho et al. 2002; Wang and Hwang 2001; Portilla et al. 2009). Here, we apply a method to obtain one-dimensional spectra, adapted from combining characteristics of different methods, which we visually judge to be appropriate to our data. We developed a criterion to select of consistent spectral peaks necessary to identify a multimodal spectrum. Spurious peaks are dependent on the observation sampling frequency and the spectral estimation method. The analysis can distinguish wide peaks from multi-peak spectrums that may represent two wave systems (Pierson 1977). In addition to eliminating spurious peaks using commonly used criteria based on minimum distance between peaks and high frequency threshold, we also

apply a 90 % confidence interval test (Guedes-Soares and Nolasco 1992). This method considers spurious peaks as a consequence of the spectral estimates. The confidence levels are calculated by a chi-squared distribution considering the number of degrees of freedom and it is applied to validate the troughs which separate two partitions. The lower confidence limit of the energy of the smaller peak must be higher than the energy of the trough between the peaks. Since we process the MRU and TriAxys to obtain the same frequency resolution, the lower confidence limits are 0.65 and 0.72, respectively.

The steps used to identify significant peaks are:

- (1) peaks must be below the high frequency threshold of 0.4 Hz;
- (2) peak energy density of smaller peaks must be higher than 7 % of the next higher peak. Peaks below this limit were visually considered insignificant.
- (3) distance between peaks must be at least 0.03 Hz, which corresponds to $3df$ (where df is the frequency resolution).
- (4) 90 % confidence interval test: lower peak is excluded if the trough between two peaks is less than the lower limit of the confidence interval of the lower peak.

2.3 Wind-Sea identification

After identifying significant spectral peaks, we classified each wave system into swell or wind-sea. It is implicit in the definition that swells are waves, formerly generated by the wind, but no longer receiving energy from the local wind. Such conditions certainly occur when the waves travel outside the area of generation. It is generally accepted that such conditions can be identified by the relative wind/wave speed, i.e., swell waves travel faster than the wind, or wind/wave angle, e.g., waves propagating at angles greater than 90 degrees with the wind direction cannot receive energy from the local wind.

While such indicators make physical sense, it has been shown that in general they do not necessarily signify wind/wave decoupling. A number of studies have tested the commonly used premise that swell is the wave system which no longer evolves or receives energy. Thomson and Rogers (2014), for example, showed that waves well under the Pierson-Moskowitz limit, i.e., traveling much faster than the local wind, fit perfectly the dependence of dimensionless energy and fetch for wave-growth. Young (2006), when investigating wave evolution in tropical cyclones, achieved a similar conclusion. The spectra showed no distinction between spectral peaks. The different "quadrants" of the hurricane present a complex swell and sea "mixed" system in a continuous spectrum. Moreover, he found that waves at angles as large as 90 and even 180 degrees to the wind

(in different quadrants of the hurricane) satisfy the JON-SWAP spectrum of wind-generated waves very well.

These considerations increase the complexity of wind-sea classification. Different methods have been proposed to identify the wind-sea partition of the spectrum. The most common is based on the inverse wave age (U_{10}/c_p , where c_p is the phase velocity of the wave peak frequency and U_{10} is the wind speed at 10 m height) using wind speed information. Different limits have been applied, for example, (Donelan et al. 1985) proposed: $U_{10}/c_p > 0.83$ that allows the phase speed of local generated waves to exceed the wind speed. The Pierson and Moskowitz (1964) asymptotic limit of wave development is also often used, $\nu = f_p U_{10}/g > 0.13$, which represents a $U_{10}/c_p > 0.8$. Other authors (e.g., Thomson and Rogers 2014) applied the limit equal to 1, i.e., wind-sea waves cannot run faster than the winds. If the wind speed is not available, different techniques have also been proposed such as wave steepness-based methods (e.g., Gilhousen and Hervey 2001; Wang and Hwang 2001) and the spectrum integration method proposed by Hwang et al. (2012).

The SOFS observations include wind magnitude and direction that are used to identify the wind-sea. The data were recorded by the Air-Sea Interaction METeorology (ASIMET) Sonic Wind Module based on a high resolution (0.01 m/s, 0.1 deg) two-dimensional sonic anemometer installed on the top of the buoy tower, at a height of 3.52 m above the sea-surface. The wind data were recorded as 1-min averages and then averaged over the same 10 min as the MRU sensor observations, for SOFS-1, and over the 20 min used by the TriAxys sensor, for SOFS-2 and 4. The conversion from the wind measurement height of 3.52 to 10m above the water was done by applying a sea drag coefficient suitable for high wind speeds (Hwang 2011): $C_D \times 10^{-4} = 8.058 + 0.967U_{10} - 0.016U_{10}^2$.

Our approach to identifying the wind-sea peak is based on two requirements. The inverse wave age (U_{10}/c_p) must be greater than 0.8 and the mean direction corresponding to the wave peak frequency θ_p must be less than +/- 90° of the wind direction. This directional criteria is based on the Komen's formula (Komen et al. 1984), which has been used in different two-dimensional spectral partitioning to identify wind-sea region (e.g., Voorrips et al. 1997):

$$1.3 \frac{u_z}{c_p} \cos(\phi) > 1 \tag{6}$$

where u_z is the wind speed at height z and ϕ is the angle difference between wind and wave directions. The maximum angle ϕ tends to 90° as the wind velocity u_z tends to infinity (Fig. 5). Therefore, the directional condition applied in our method is only restrictive for waves traveling exactly perpendicular or contrary to the wind.

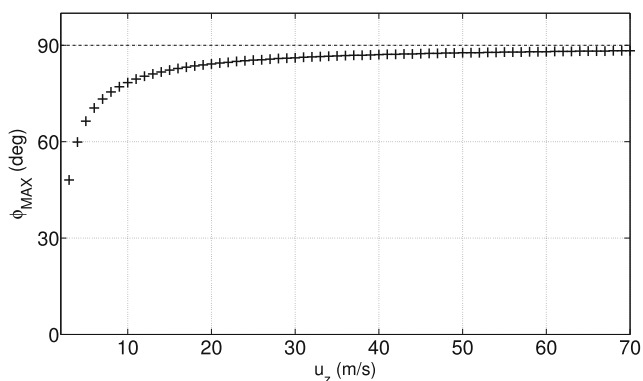


Fig. 5 Maximum angle between wind and wave directions (ϕ_{MAX}) as a function of the wind speed u_z according to Eq. 6

3 Results

3.1 Wave parameters statistics

A statistical analysis of the main wave characteristics is obtained using the parameters of zero-moment wave height H_{m0} , peak period T_p , and mean direction corresponding to the spectral peak θ_p . The analysis of T_p and T_{m01} reveal very similar statistics and here we show only results for T_p since it is more commonly used to characterize the sea state. The statistics are based on the mean value, standard deviation, and maxima occurred. Firstly, the one-dimensional parameters of H_{m0} and T_p will be analyzed, followed by a description of methods and results of the analysis of θ_p . All the results presented in this section are shown for each deployment and for the whole data set. It is worth noting that the first deployment is more representative since it covered an almost full year (10 months), and hence all seasons. SOFS-2 and SOFS-4 spanned 9 and 7 months, respectively.

The probability distribution function (PDF) of significant wave height and peak period is shown in Fig. 6 for each deployment. Previous studies have attempted to model distributions of wave height and period, as for example, the notable works of Forristal (1978) and Longuet-Higgins (1975). The description of the tail is particularly important for engineering design. Several studies have been performed to describe and model H_s and T_p distributions (e.g., Ferreira and Soares 2000), including analysis of H_s for the Southern Ocean (Young 1994).

Distributions of wave height have been commonly associated with a theoretical Rayleigh or Weibull distribution, which the probability density functions of a variable ξ are expressed, respectively, by:

$$p(\xi) = \frac{\xi}{a^2} e^{-\frac{\xi^2}{2a^2}}$$

$$p(\xi) = \frac{b}{a} \left(\frac{\xi}{a}\right)^{b-1} e^{-\left(\frac{\xi}{a}\right)^b} \tag{7}$$

where a and b are scale and shape parameters, respectively. A normal-type distribution has been applied to characterize wave period:

$$p(\xi) = \frac{1}{\sigma\sqrt{2\pi}} e^{-\frac{(\xi-\mu)^2}{2\sigma^2}} \tag{8}$$

where μ and σ are mean and standard deviation, respectively. The normalized distribution for H_{m0} and T_p corresponding to the full data set are shown in Fig. 7. Weibull and Rayleigh curves are plotted in comparison with H_{m0} and a normal fit is shown with the T_p distribution. The right-side plots show the exceedance probability in attempt to represent the best fit for the upper tail.

Fig. 6 H_{m0} (top panels) and T_p (bottom) Probability Density Function (PDF) distributions for the three deployments. Distributions are from SOFS-1 (left), SOFS-2 (centre), and SOFS-4 (right)

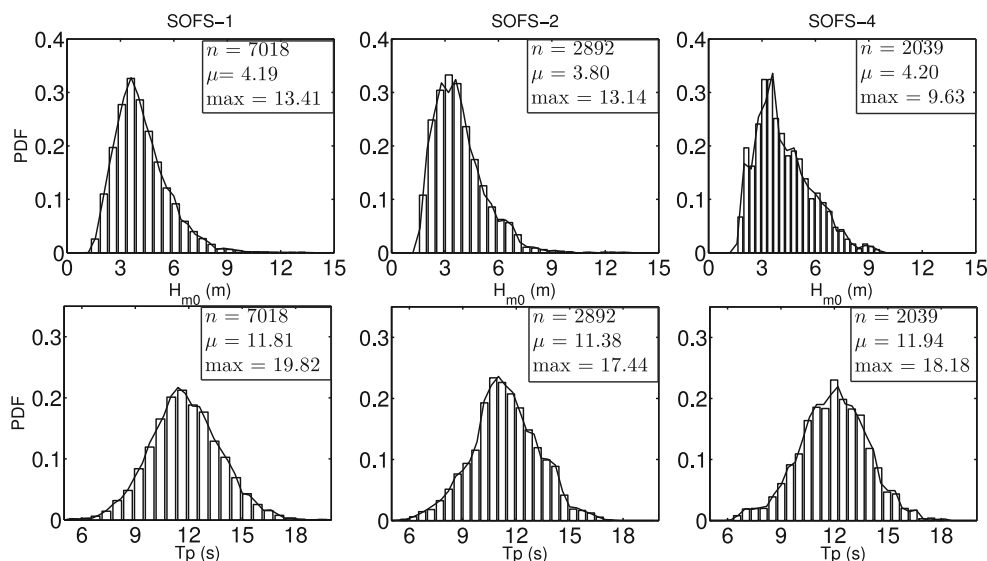
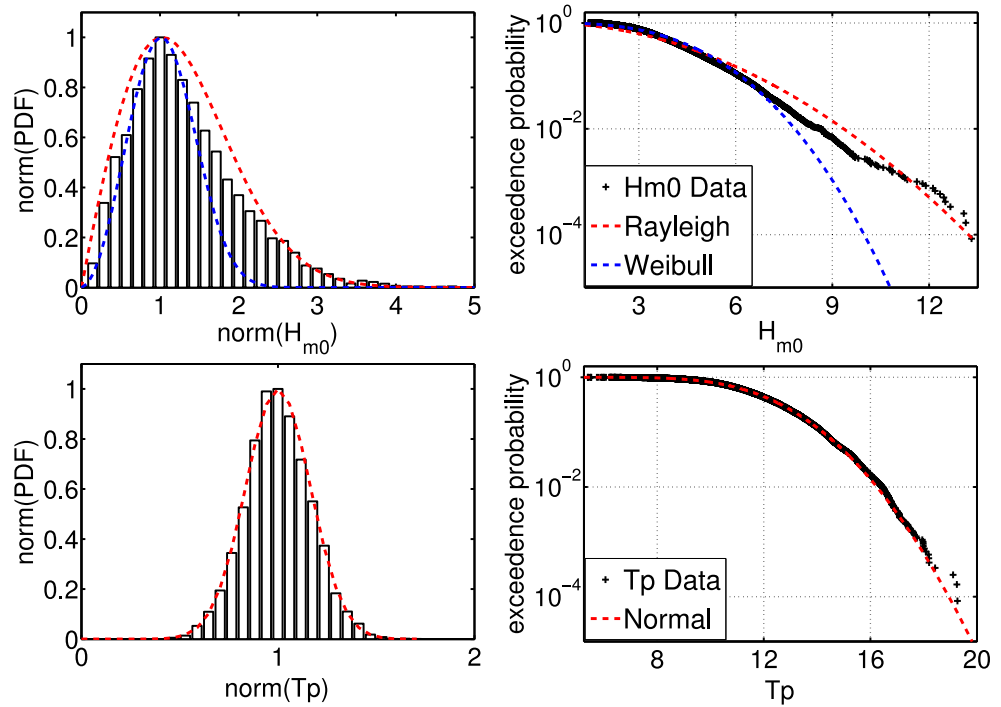


Fig. 7 Comparison of Rayleigh and Weibull distribution for H_{m0} (top panels) and Normal distribution for T_p (bottom panels) for the full SOFS data set. Left plots are normalized PDF and right plots show exceedance probability



From the top-right panel, we can see that a Rayleigh distribution provides a better fit to this data than a Weibull distribution. However, both models were unable to fully represent the upper tail. The normal fit agrees well with the peak period distribution obtained from the SOFS data. The bottom-right panel shows that tail is well represented. The aim of this study is to show if typically applied models are in good agreement with the data rather than modeling the distribution for wave parameters. Further analysis will be necessary to determine if other proposed methods are suitable to represent the SO wave parameters distribution. The individual wave height and period distributions are a subject for future analysis.

Table 2 summarizes the main statistical parameters (mean value μ , standard deviation σ , and maxima) as well

as the date of the most extreme events in terms of H_{m0} found for each deployment and for the full data set. The three deployments are very consistent in terms of wave parameters statistics (Table 2). The mean H_{m0} for the full data set was 4.09 m. SOFS-2 showed mean H_{m0} 0.4 lower than the other deployments (SOFS-1 and SOFS-4).

The highest waves occurred during the austral spring (SOFS-1 and 4) and autumn (SOFS-2). The maximum H_{m0} found was 13.41 m and occurred during SOFS-1, in September 2010. A very similar value was measured in April 2012 when SOFS-2 was in the water. SOFS-4 was operational for these two respective months of 2013; however, the maximum H_{m0} obtained was 9.63 m. It is worth noting that SOFS-2 was not deployed during September, when maximum H_{m0} was found for the other deployments.

Table 2 Statistics of each deployment: mean value (μ), standard deviation (σ), maximum (max), and minimum (min)

	H_{m0} (m)				T_p (s)				θ_p (deg)		
	μ	σ	max	Date of max	μ	σ	max	min	μ	σ	$\theta_p[\max(H_{m0})]$
SOFS-1	4.19	1.49	13.41	16-Sep-10	11.81	1.96	19.82	4.87	241.6	38.5	241
SOFS-2	3.80	1.40	13.14	28-Apr-12	11.38	1.87	17.44	5.50	233.7	33.8	240
SOFS-4	4.20	1.55	9.63	30-Sep-13	11.94	1.91	18.18	6.30	241.3	33.8	243
All	4.09	1.49	13.41	16-Sep-10	11.73	1.94	19.82	4.87	239.6	36.8	241

$\theta_p[\max(H_{m0})]$ is the mean wave direction associated with the maximum H_{m0} event

To calculate the mean wave direction a vector analysis was applied:

$$\bar{u}_\theta = n^{-1} \sum_{i=1}^n \cos(\theta_i),$$

$$\bar{v}_\theta = n^{-1} \sum_{i=1}^n \sin(\theta_i), \tag{9}$$

where n is the number of samples and θ_i is direction in the trigonometric convention (i.e., counter-clockwise with $0^\circ =$ east). The mean direction is then obtained by:

$$\mu_\theta = \arctan(\bar{v}_\theta / \bar{u}_\theta) \tag{10}$$

The standard deviation was calculated following Yamartino’s method (Yamartino 1984) for wind direction:

$$\sigma_\theta = \arcsin(\epsilon) \left[1 + (2/\sqrt{3} - 1) \epsilon^3 \right] \tag{11}$$

where

$$\epsilon = \sqrt{1 - (\bar{u}_\theta^2 + \bar{v}_\theta^2)} \tag{12}$$

The distributions of mean direction associated with the peak frequency (θ_p) (Fig. 8) are very similar for the three deployments. Similarly, mean (μ) and standard deviation (σ) are consistent for all deployments. Waves predominantly come from the southwest (SW) direction. Waves from south/southeast (S/SE) and northwest (NW) were also observed. The second quadrant waves, i.e., from east/northeast (E/NE), were very infrequent (accounted only for 1.5 % of observations) and associated with small H_{m0} values. S/SE waves were observed mainly during austral summer (Dec–Feb), particularly during the SOFS-1 deployment (2010–2011). This deployment exhibited a higher standard deviation as a consequence of more frequent waves from SE and NW, and it was the only deployment to span all seasons. The relative intensity (H_{m0}) for the direction segments shown in Fig. 8 reveals that the higher waves are concentrated in the SW direction. From Table 2, we can see the most extreme events in terms of H_{m0} had a consistent direction of around 240° .

The two most extreme events measured in terms of zero-moment wave height were very similar. The first event ($H_{m0} = 13.41$) occurred during the SOFS-1 deployment and was only recorded by the MRU. For the second event ($H_{m0} = 13.14$ m) both the MRU and TriAxes were operational, providing a good opportunity to compare their performance during large waves. Figure 9 shows wave parameters of zero-moment wave height, peak period and peak direction for both sensors during the second highest event. We can observe that both sensors performed well and recorded the evolution of the three wave parameters with good agreement except for the recorded maximum value, where the MRU recorded a significant wave height of 15.2 m, while TriAxes analysis resulted in 13.14 m. From

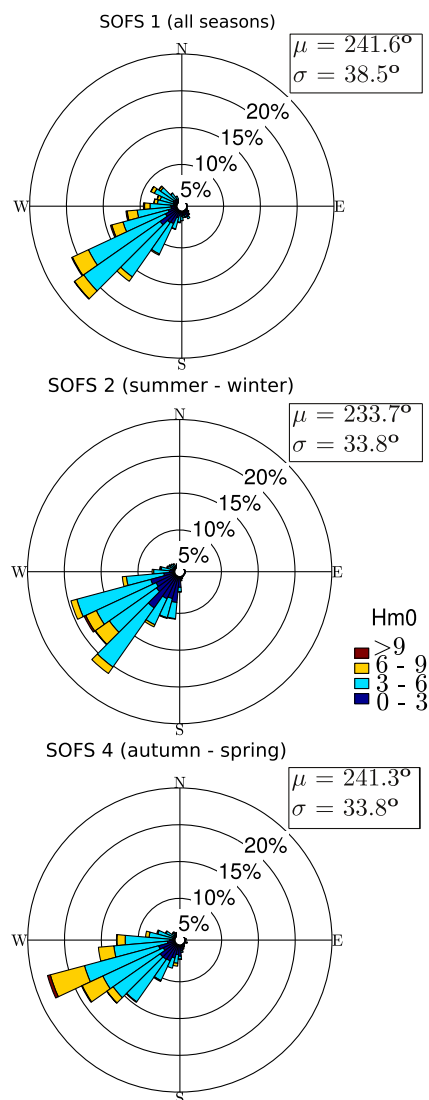


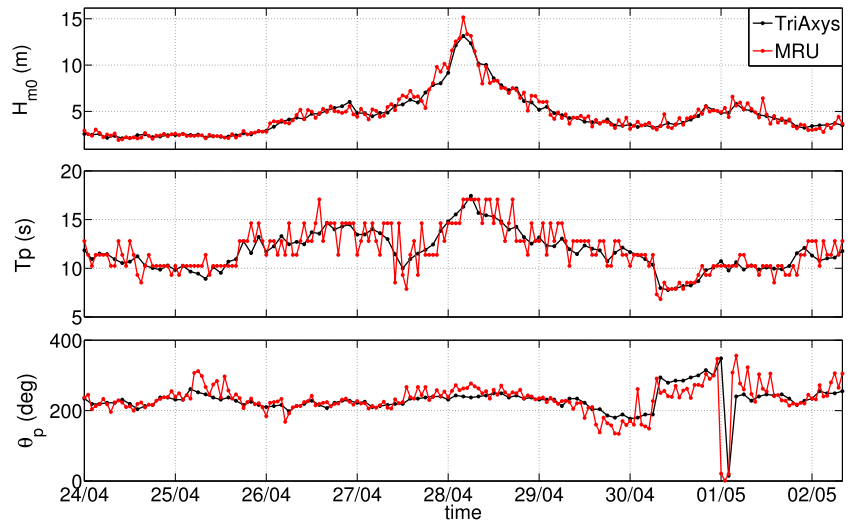
Fig. 8 Mean Direction corresponding to the spectral peak (θ_p) distribution for the three deployments. The plots represent the direction where the waves come from and the bar color scale is H_{m0} . The austral seasons covered by the deployments are indicated within parentheses of each plot’s title

this difference, we can suppose that the first event measured during SOFS-1, when MRU recorded a H_{m0} of 13.41, may actually have been the second highest event. Unfortunately, we do not have a second sensor for comparison and as both events presented similar characteristics it is not possible to conclude which one was the highest. We however keep the assumption that TriAxes is the ground truth measurement when available, based on the longer time series and higher confidence level of the spectral estimates.

3.2 Wave system analysis

The analysis of wave parameters have shown the main characteristics of waves and sea severity during the years

Fig. 9 Zero-moment wave height H_{m0} , peak period T_p , and peak direction θ_p from the MRU and TriAxys, for the second highest event measured at the Southern Ocean Flux Station during SOFS-2 on 28 April 2012



covered by the three deployments. In order to have a broader understanding of the wave patterns in the Southern Ocean, we now show the results of the characterization of wave systems commonly found through the analysis of each individual spectrum.

The spectra were generally classified as exhibiting either one or two peaks. The predominance of swell or wind-sea systems varied for both cases and will also be discussed in this section. Three-peak spectra were also identified, however, very few of them passed the selection process (Section 2). We considered any fourth peaks as a spurious or insignificant wave system for the analysis. It is worth noting that due to the regular presence of westerly winds with reasonable intensity in the SO, a certain amount of high frequency energy is often seen. However, most of these peaks, which represent a wind-sea in early stages of development, did not satisfy the conditions imposed in the peak identification method described in section 2 and consequently they were not taken into account. Examples of 1, 2, and 3 peak spectra and the identification of the frequency for each peak are shown in Fig. 10.

Table 3 shows the total number of spectra analyzed and classified into categories according to the number of peaks, for each deployment and for the whole data set. The predominance of 1 peak cases is clear (71 %), followed by

double-peaked spectra (26 %) and a small number of 3 peaks (3 %). All spectra were visually checked.

Following the spectral characterization by the number of peaks, we performed the identification of a possible wind-sea system. In the SO, the wind is predominantly from W/SW. As shown previously, waves have a similar directional behavior. Therefore, the directional requirement for wind-sea identification is often fulfilled by the dominant waves. The limitation comes with the wave age limit.

After this step, we could classify each spectrum into swell or wind-sea dominated. The results are also shown in Table 3. The number and relative participation (values within parentheses) of swell dominated spectra (“Swell Dom.” in the table) is also shown. A notable characteristic is the higher relative participation of swell dominated spectra for all cases, peaking at 93 % of unimodal cases during SOFS-4. Overall, the relative participation of swell dominated spectra was 85, 83, and 73 % for 1, 2, and 3 peak spectra, respectively.

Examples of typical wind-sea and swell-dominated bimodal spectra are shown in Fig. 11. The case selected provides a good example of alternating swell and wind-sea dominance in a local wave growth event. The three plots, from left to right, represent the time evolution of the wave spectrum, plotted together with the wave mean direction

Fig. 10 Examples of 1, 2, and 3 peak spectra. The dashed lines show the peaks identified using the method described in Section 2

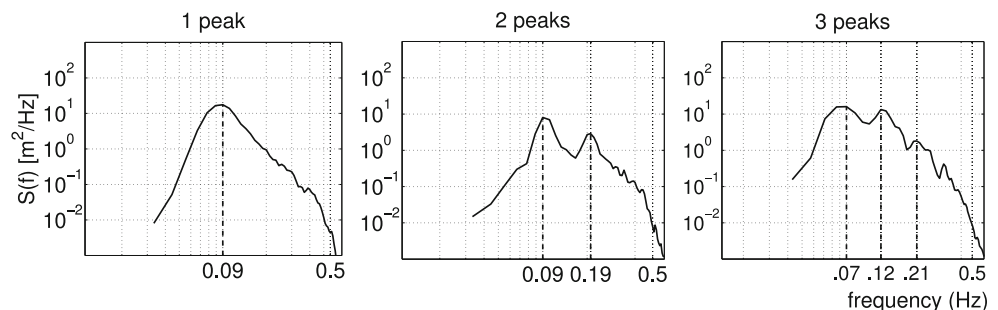


Table 3 Distribution of analyzed spectra according to the number of peaks and swell dominated cases (“Swell Dom”)

	Number of Spectra	1 peak		2 peaks		3 peaks	
		Total	Swell Dom.	Total	Swell Dom.	Total	Swell Dom.
SOFS-1	7018	4653 (0.66)	3894 (0.84)	2064 (0.30)	1687 (0.82)	301 (0.04)	210 (0.70)
SOFS-2	2841	2274 (0.80)	1897 (0.83)	541 (0.19)	431 (0.80)	26 (0.01)	20 (0.77)
SOFS-4	2017	1451 (0.72)	1360 (0.93)	514 (0.25)	468 (0.91)	52 (0.03)	45 (0.87)
All	11876	8378 (0.71)	7151 (0.85)	3119 (0.26)	2586 (0.83)	379 (0.03)	275 (0.73)

The values in parentheses correspond to the relative occurrence

$\theta_0(f)$ and averaged wind direction over the wave record length used to calculate each spectrum. The wind-sea component is generated by northwest winds (this is the mean wind direction over the time used to calculate the spectrum and represented by the gray dashed line). A swell system is also present coming from the southwest. As the wind-sea evolves the swell loses energy and at some stage, the local system surpasses the swell in energy, thus becoming dominant. The evolution of the wind-sea in this case shows another interesting feature. The wind shifts progressively up to 279° during the spectrum evolution. The angle between the locally generated waves and local wind reaches 40° in the last spectrum, however, the wind-sea keeps receiving energy and growing.

Figure 12 shows the dimensionless peak frequency $\nu = U_{10} f_p / g$ as a function of dimensionless energy, $\varepsilon = g^2 m_0 / U_{10}^4$, only for the unimodal cases. Swell and sea are plotted with different markers. Donelan et al. (1985) proposed the dependence:

$$\varepsilon = 6.365 \times 10^{-6} \nu^{-3.3} \quad (13)$$

Babanin and Soloviev (1998) empirically found the relation:

$$\varepsilon = 8.30 \times 10^{-6} \nu^{-3.01} \quad (14)$$

Dependencies from Eqs. 13 and 14 are plotted together with the SO results. The vertical dashed line delimits the P-M limit. The agreement with the relation proposed by Donelan et al. (1985) is good, and interestingly swell and sea seem to show similar dependencies, with no clear difference in the behavior of each system. However, this relation (and others, e.g., Dobson et al. 1989) is based on the -3.3 power assumed in Hasselmann et al. (1976) and not empirically obtained. Dependencies empirically proposed by other authors show lower absolute values than -3.3 for the power of ν , e.g., -2.94 in Evans and Kibblewhite (1990) and -3.00 by Kahma (1981). From Fig. 12, we can see that the SO data exhibit a higher power than 3.3, which suggest that the nature of air-sea interactions and wave evolution might be different in the extreme wind conditions found in the Southern Ocean. A more thorough investigation and careful selection of the spectra are necessary to obtain a representative dependence for dimensionless wave energy and peak frequency for the SO.

The swell dominated characteristics of the wave field described above are consistent with Fan et al. (2014) who suggest swell fractions of 0.6–0.7 on the northern edge of the SO storm belt at which SOFS is located. However, this

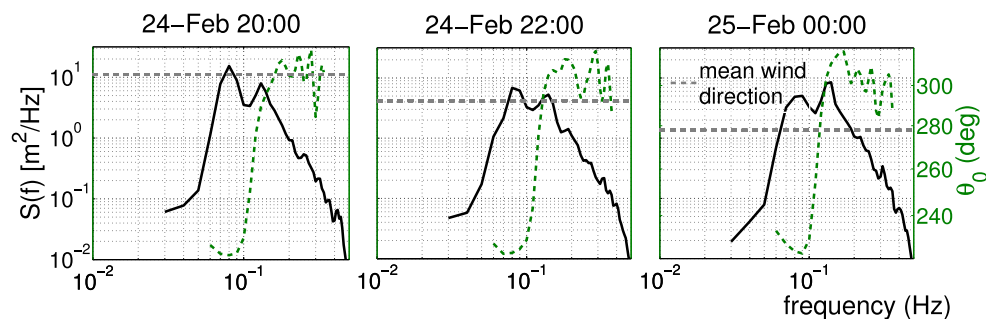


Fig. 11 Example of time evolution of wind-sea in a bimodal case during February 2012. The *green dashed line* shows mean direction and *gray dashed line* is averaged wind direction over the 20 min used by the

TriAxis sensor to calculate the wave spectrum. Corresponding averaged wind speed for the three plots, from left to right, are 11.78, 9.22, and 11.17 m/s, respectively

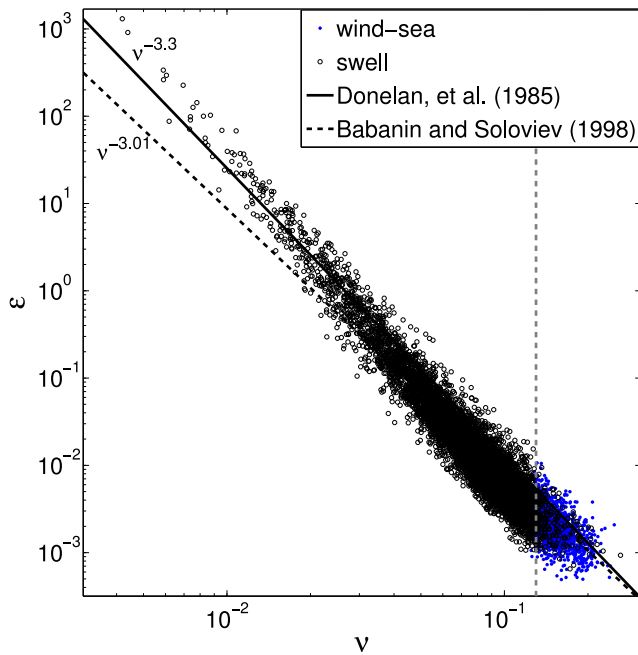


Fig. 12 Dimensionless energy ε versus dimensionless frequency ν for unimodal cases. *Black circles* are swell dominated cases and *blue solid dots* wind-sea. *Solid and dashed black lines* represent dependencies from equation 11 (Donelan et al. 1985) and 12 (Babanin and Soloviev 1998), respectively. *Vertical gray dashed line* draws the Pierson-Moskowitz limit for wind-sea. The power of ν for both dependencies are shown beside each line

may be a simplification of the dynamics which occur at the SOFS site. Wave generation occurs in the Southern Ocean, and the noted dominance of swell over wind-sea should possibly be interpreted carefully. The SOFS location is exposed to a long fetch for the prevailing wind and waves to the west and the amount of wave energy is often high, as well as their dominant periods, as can be seen from the wave

parameters statistical analysis (Section 3.1). The development of locally-generated waves is likely to often be in advanced stages and a slight drop in wind speed or direction shift may insert these waves into a swell classification.

In Young (2006), despite the higher number of spectra dominated by swell, a “mixed” system is seen and the parameters obtained follow similar relations of wind-sea conditions. The author found no clear bimodal distribution in his analysis, similar to the cases shown in our Fig. 12, and the agreement found for dimensionless peak frequency and energy was also high. It suggests that most of our unimodal cases classified as swell might still be connected with the local wind wave system. As mentioned previously, Thomson and Rogers (2014) also did not see a clear distinction between swell and sea for the dependence of dimensionless energy and fetch. Both observations, together with the results here presented, suggest that waves, which on the basis of the formal indications mentioned above should be classified as swell, behave like wind waves. Waves faster than the wind and waves at greater angles to the wind continue receiving energy. Young (1997) argued that this is done through the nonlinear interactions: short waves are locally generated and wind-forced, and they pass energy to what should appear as swell through wave-wave exchanges. This physical mechanism is entirely plausible, and there are direct and indirect evidences supporting such conclusions.

3.3 Comparison with wave hindcast model

Our results were compared and validated against the CAWCR wave hindcast model (Durrant et al. 2013). This is the first time that the widely used NOAA WAVEWATCH III (ww3) model has been tested and validated against a long-term moored buoy in the SO. We note that the hindcast

Fig. 13 Time series of H_{m0} , T_p , and θ_p (model vs. SOFS data) for 17 March–8 June 2012 (SOFS-2)

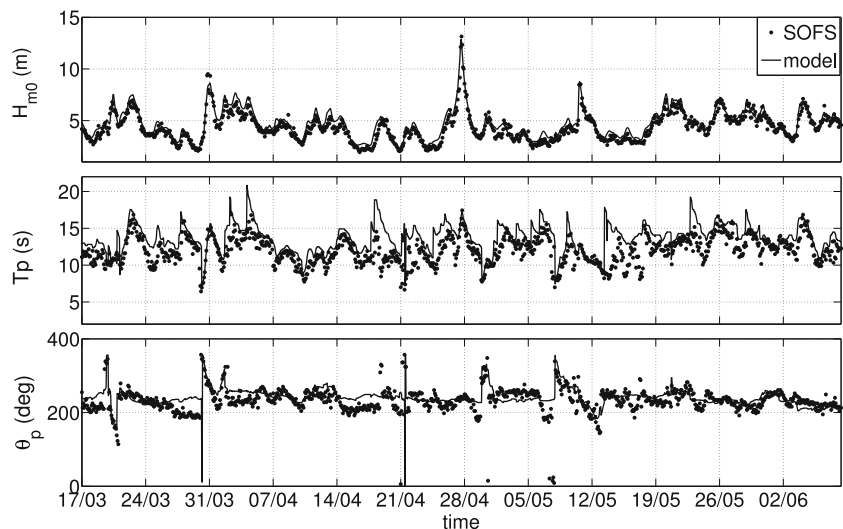
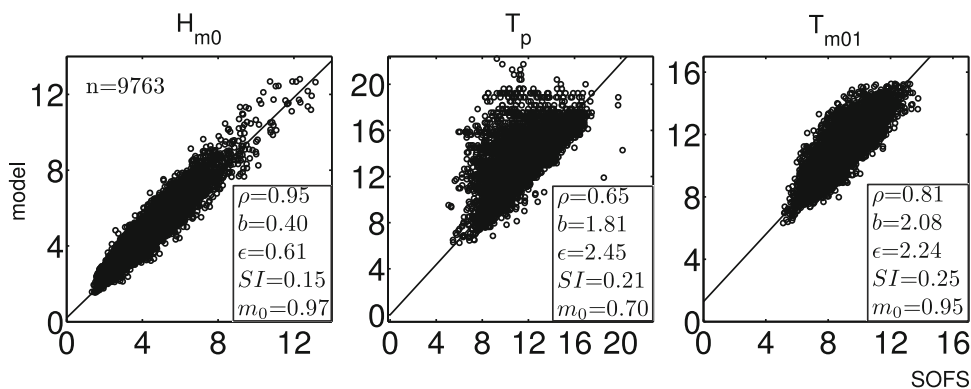


Fig. 14 Scatter plots of wave height, peak period, and mean period for the hindcast. Displayed scatter statistics are n = number of samples, ρ = Pearson’s correlation coefficient, b = bias, ϵ = root mean square error, SI = scatter index, and m_0 = slope of least-square regression



model run has not been tuned against the SOFS observations. For this, we use the parameters of H_{m0} , T_p , T_{m01} , θ_p , and θ_m , where the later is defined as:

$$\theta_m = \arctan \left[\frac{\bar{b}_1}{\bar{a}_1} \right] \tag{15}$$

where

$$\begin{aligned} \bar{a}_1 &= \frac{1}{\bar{S}} \int_0^\infty a_1(f) S(f) df \\ \bar{b}_1 &= \frac{1}{\bar{S}} \int_0^\infty b_1(f) S(f) df \end{aligned} \tag{16}$$

where $\bar{S} = \int_0^\infty S(f) df$.

The ww3 model version 4.08 was run for a $0.4^\circ \times 0.4$ global grid, forced by hourly wind fields and ice concentration from the CFSR reanalysis (Saha et al. 2010). The spectral space was discretized over 29 frequencies logarithmically spaced from 0.038 to 0.5 Hz and 24 directions with 15° resolution. The most recent official release version 4.18 was also run for a shorter period with same configuration and the results were qualitatively consistent.

To provide a sense of the performance of the model, sample time-series of H_{m0} , T_p , and θ_p are shown in Fig. 13. It includes one of the extreme events described in Section 3.1 and Fig. 9. A visual qualitative analysis suggests good agreement between for H_{m0} . The model captures the observed peak H_{m0} . The model consistently overestimates T_p compared to observations.

The scatter plots of the one-dimensional parameters H_{m0} and T_p , along with T_{m01} , for the whole data set, are shown in Fig. 14. Zero-moment wave height shows very good agreement with low bias, rms error, and scattering and high correlation. The ww3 model is designed to reproduce the integrated spectral energy and this is reflected in the H_{m0} result. Both peak and mean periods overestimate compared to the observed, with biases greater than 2 s. The correlation coefficient for T_{m01} (0.81) is however considerably better than for T_p (0.65).

Directional validations of θ_p and θ_m are shown in Fig. 15. The statistical analysis performed is based on the angle difference between model and buoy results. The presence of points on the upper left and lower right corners represent the transition of 359 to 0° and despite the distance to the regression line they actually contribute to low errors, since they represent small angle differences.

The model shows better agreement with observations for the integrated mean direction θ_m than the peak direction θ_p . The performance of θ_p depends on how well the peak frequency is identified, as pointed out by Rogers and Wang (2006). Since the modeled peak period shows some disagreement with the observations, it is expected that the peak direction will reproduce similar results. Rogers and Wang (2006) address this problem and calculate T_p as a function of T_m , which normally provides better agreement.

The modeled peak direction shows more waves from SW when the buoy data indicates SSE or NW. This can be seen by the horizontal line of points around 240° in the scatter plot (left panel of Fig. 15). Further investigation of a sample of these cases revealed that the NW measured cases are related to bimodal wind-sea dominated spectra which the model does not represent. Cases where the buoy θ_p is SSE while the model outputs SW peak directions are normally unimodal swell dominated spectra. These differences might

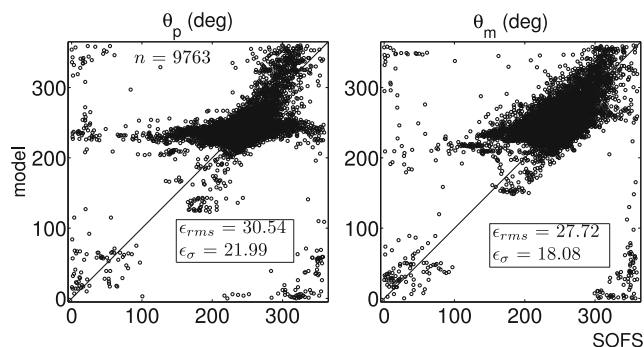


Fig. 15 Scatter plots of peak and mean direction for the hindcast. The statistical parameters are represented by ϵ_{rms} = root mean square error of the angle difference; and ϵ_σ = standard deviation of the angle difference

be associated with current-induced refraction and requires further investigation.

The mean direction is the most common parameter used to characterize wave directional properties in models. The standard calculation of this parameter by *ww3* is done by integrating the mean direction θ_0 over all frequencies. The results show better agreement than θ_p . Rogers and Wang (2006) also found improved agreement using an alternative method to validate wave direction by integrating θ_m over frequencies near the spectral peak. It is common to see low and high frequency waves coming from similar directions in the Southern Ocean. Therefore, the use of a narrower band of frequencies might not show significant differences, however, this is the subject of future research.

4 Conclusions

The results presented provide the first wave analysis from a long-term buoy deployed in a remote area of the Southern Ocean. Westerly winds are consistently strong at the mooring site, and this is reflected in the consistent wave statistics that show little variation across the three deployment periods. The waves come predominately from southwest/west, with mean significant wave height of 4.1 m. The highest wave event recorded was $H_{m0} = 13.41$ m.

The wave parameters were used to validate the CAWCR wave hindcast, which showed good agreement for significant wave height, but considerable positive biases for peak and mean period. This data set will be valuable for calibration of future wave models in the Southern Hemisphere.

The characterization of the measured spectra shows a predominance of unimodal cases (71 %). Bimodal spectra were reasonably common (26 %), followed by a small numbers of trimodal cases (3 %). Applying a method of wind-sea identification based on the wind direction and wave age, we found a high relative participation of swell dominated conditions (84 % of all spectra). These results however might not reflect the strong wave generation characteristics of the SO. The techniques used here are not designed to investigate the generation of wind waves which we suspect is vigorous in the Southern Ocean. This data set offers an excellent opportunity to revisit and improve the knowledge regarding swell–sea relations and to investigate wave growth under strong wind conditions.

The goal of this paper is to present the main statistics and spectral characterization of the wind-generated waves from the floating mooring motion recorded in the three first successful deployments. The data set recorded by the Southern Ocean Flux Station includes additional meteo-oceanographic parameters such as: acoustic current profilers, wind, radiation, and parameters for computing

bulk air-sea fluxes, ocean turbulence, and biogeochemical sensors. SOFS-5 is currently in the water and the project is expected to continue in the coming years. The opportunity to analyze long-term in situ data from one of the most remote and poorly sampled oceans will enable a great number of research activities in the near future.

Acknowledgments We are very thankful to the CSIRO and National Marine Facility group involved in the SOFS mooring, especially to Peter Janssen. We thank the crew who supported the operations on board and have made the project successful so far. Data were sourced from the Integrated Marine Observing System (IMOS)—IMOS is a national collaborative research infrastructure, supported by Australian Government. We acknowledge funding from NCRIS IMOS and the CSIRO collaboration development fund.

References

- Alves JHGM (2006) Numerical modeling of ocean swell contributions to the global wind-wave climate. *Ocean Model* 11:98–122
- Babanin AV, Soloviev YP (1998) Field investigation of transformation of the wind wave frequency spectrum with fetch and the stage of development. *J Phys Oceanogr* 28:563–576
- Badulin SI, Babanin AV, Zakharov VE, Resio D (2007) Weakly turbulent laws of wind-wave growth. *J Fluid Mech* 591:339–378
- Benoit M, Frigaard P, Schffer HA (1997) Analysing multidirectional wave spectra: a tentative classification of available methods. In: *Proceedings on the International Association of Hydraulic Engineering and Research: Multidirectional Waves and Their Interaction with Structures*, San Francisco, CA, pp 131–157
- Dobson F, Perrie W, Toulany B (1989) On the deep-water fetch laws for wind-generated surface gravity waves. *Atmos Ocean* 27:210–236
- Donelan MA, Hamilton J, Hui WH (1985) Directional spectra of wind-generated waves. *Philos Trans R Soc London* 315:509–562
- Donelan MA, Babanin AV, Young IR, Banner ML (2006) Wave follower measurements of the wind input spectral function, part 2. Parameterization of the wind input. *J Phys Oceanogr* 36:1672–1688
- Durrant T, Hemer M, Trenham C, Greensdale D (2013) CAWCR wave hindcast extension jan 2011 - may 2013. v4. CSIRO, data Collection. doi:10.4225/08/52817E2858340
- Evans KC, Kibblewhite AC (1990) An examination of fetch-limited wave growth off the west coast of new zealand by a comparison with the jonswap results. *J Phys Oceanogr* 20:1278–1296
- Fan Y, Lin SJ, Griffies SM, Hemer M (2014) Simulated global swell and wind-sea climate and their responses to anthropogenic climate change at the end of the twenty-first century. *J Climate* 27:3516–3536
- Ferreira JA, Soares CG (2000) Modelling distributions of significant wave height. *Coastal Eng* 40:361–374
- Forristal GZ (1978) On the statistical distribution of wave heights in a storm. *J Geophys Res* 83(C5):2353–1358
- Gilhousen DB, Hervey R (2001) Improved estimates of swell from moored buoys. In: *Proceedings of the Fourth International Symposium WAVES 2001*, ASCE, Alexandria, VA, pp 387–393
- Guedes-Soares C, Nolasco MC (1992) Spectral modelling of sea states with multiple wave systems. *J Offshore Mech Arctic Eng* 114:278–284
- Hasselmann K, Ross DB, Muller P, Sell W (1976) A parametric wave prediction model. *J Phys Oceanogr* 6:200–228

- Hemer MA (2010) Historical trends in southern ocean storminess: long-term variability of extreme wave heights at cape sorell, tasmania. *Geophys Res Lett* 37(L18601). doi:[10.1029/2010GL044595](https://doi.org/10.1029/2010GL044595)
- Hemer MA, Church JA, Hunter JR (2009) Variability and trends in the directional wave climate of the Southern Hemisphere. *Int J Climatol* 30(4):475–491. doi:[10.1002/joc.1900](https://doi.org/10.1002/joc.1900)
- Hwang PA (2011) A note on the ocean surface roughness spectrum. *J Atmos Oceanic Technol* 28:436–443
- Hwang PA, Ocampo-Torres FJ, Garcia-Nava H (2012) Wind sea and swell separation of 1d wave spectrum by a spectrum integration method. *J Atmos Oceanic Technol* 129:116–128. doi:[10.1175/JTECH-D-11-00075.1](https://doi.org/10.1175/JTECH-D-11-00075.1)
- Kahma KK (1981) A study of the growth of the wave spectrum with fetch. *J Phys Oceanogr* 11:1503–1515
- Komen GJ, Hasselmann S, Hasselmann K (1984) On the existence of a fully developed windsea spectrum. *J Phys Oceanogr* 14:1271–1285
- Longuet-Higgins MS (1975) On the joint distribution of the periods and amplitudes sea waves. *J Geophys Res* 80(18):2688–2694
- Lygre A, Krogstad HE (1986) Maximum entropy estimation of the directional distribution in ocean wave spectra. *J Phys Oceanogr* 16:2052–2060
- Meyers G (2008) The australian integrated marine observing system. *J Atmos Oceanic Technol* 3:80–81
- Mognard NM, Campbell WJ, Cheney RE, Marsh JG (1983) Southern ocean mean monthly waves and surface winds for winter 1978 by Seasat radar altimeter. *J Geophys Res* 88(C3):1736–1744
- Orsi AH, Johnson GC, Bullister JL (1999) Circulation, mixing and production of antarctic bottom water. *Prog Oceanogr* 43:55–109
- Pearson K (1896) Mathematical contributions to the theory of evolution. III. regression, heredity and panmixia. *Philos Trans R Soc Lond B* 187:253–318
- Pierson WJ (1977) Comments on 'a parametric wave prediction model'. *J Phys Oceanogr* 7:127–134
- Pierson WJ, Moskowitz L (1964) A proposed spectral form for fully developed wind seas based on the similarity theory of s. a. kitaigorodskii. *J Geophys Res* 69:5181–5190
- Portilla J, Ocampo-Torres FJ, Monbaliu J (2009) Spectral partitioning and identification of wind sea and swell. *J Atmos Oceanic Technol* 26:107–122. doi:[10.1175/2008JTECH0609.1](https://doi.org/10.1175/2008JTECH0609.1)
- Powell MD, Vickery PJ, Reinhold TA (2003) Reduced drag coefficient for high wind speeds in tropical cyclones. *Nature* 422:279–283
- Rintoul SR, Sokolov S (2001) Baroclinic transport variability of the antarctic circumpolar current south of australia (WOCE repeat section sr3). *J Geophys Res* 106:2795–2814
- Rogers WE, Wang DW (2006) Directional validation of wave predictions. *J Atmos Oceanic Technol* 24:504–520. doi:[10.1175/JTECH1990.1](https://doi.org/10.1175/JTECH1990.1)
- Saha S et al. (2010) The ncep climate forecast system reanalysis. *Bull Amer Meteor Soc* 91:1015–1057. doi:[10.1175/2010BAMS3001.1](https://doi.org/10.1175/2010BAMS3001.1)
- Schulz E, Grosenbaugh MA, Pender L, Trull DJMGTW (2011) Mooring design using wave-state estimate from the southern ocean. *J Atmos Oceanic Technol* 28:1351–1360. doi:[10.1175/JTECH-D-10-05033.1](https://doi.org/10.1175/JTECH-D-10-05033.1)
- Schulz E, Josey SA, Verein R (2012) First air-sea flux mooring measurements in the southern ocean. *Geophys Res Lett* 39:8p. doi:[10.1029/2012GL052290](https://doi.org/10.1029/2012GL052290)
- Thomson J, Rogers WE (2014) Swell and sea in the emerging arctic ocean. *Geophys Res Lett*:41. doi:[10.1002/2014GL059983](https://doi.org/10.1002/2014GL059983)
- Trull TW, Schulz EW, Bray SG, Pender L, McLaughlan D, Tilbrook B (2010) The australian integrated marine observing system southern ocean time series facility. In: *Proceedings of the IEEE OCEANS 2010 Conference, Sydney*, p 7
- Violante-Carvalho N, Parente CE, Robinson IS, Nunes LMP (2002) On the growth of wind generated waves in a swell dominated region in the South Atlantic. *J Offshore Mech Arctic Eng* 124:14–21
- Voorrips AC, Makin VK, Hasselmann S (1997) Assimilation of wave spectra from pitch-and-roll buoys in a north sea wave model. *J Geophys Res* 102(C3):5829–5849
- Wang DW, Hwang PA (2001) An operational method for separating wind sea and swell from ocean wave spectra. *J Atmos Oceanic Technol* 18:2052–2062
- Welch PD (1967) The use of fast fourier transform for the estimation of power spectra: a method based on time averaging over short, modified periodograms. In: *IEEE Trans. Audio Electroacoust.*, 3p
- Yamartino RJ (1984) A comparison of several single-pass estimators of the standard deviation of wind direction. *J Climate Appl Meteor* 23:1362–1366
- Young IR (1994) Global ocean wave statistics obtained from satellite observations. *Appl Ocean Res* 16:235–248
- Young IR (1997) Observations of the spectra of hurricane generated waves. *Ocean Eng* 25:261–276
- Young IR (2006) Directional spectra of hurricane wind waves. *J Geophys Res* 111:14p. doi:[10.1029/2006JC003540](https://doi.org/10.1029/2006JC003540)